Available online at www.sciencedirect.com
ScienceDirect
Journal of Catalysis 244 (2006) 24–32
JOURNAL OF CATALYSIS
www.elsevier.com/locate/jcat

CO hydrogenation over cobalt and iron catalysts supported over multiwall carbon nanotubes: Effect of preparation

László Guczi [a], G. Stefler [b], O. Geszti [a], Zs. Koppány [a], Z. Kónya [c,*], É. Molnár [c], M. Urbán [c], I. Kiricsi [c]

[a] *Institute of Isotopes, Hungarian Academy of Sciences, P.O. Box 77, H-1525 Budapest, Hungary*
[b] *Research Institute for Technical Physics and Materials Sciences, P.O. Box 49, H-1525 Budapest, Hungary*
[c] *Applied and Environmental Chemistry Department, University of Szeged, Rerrich Béla tér 1, H-6723 Szeged, Hungary*

Received 20 June 2006; revised 9 August 2006; accepted 16 August 2006

Available online 26 September 2006

Abstract

CO hydrogenation was investigated over Co or Fe catalysts supported on multiwall carbon nanotubes (MWNTs). Two types of catalysts were prepared. For the simple impregnation method, metal acetate precursors were deposited onto the surface of MWNTs. These catalysts were denoted as "I-samples." The second family of catalysts was prepared by deposition of preprepared metal oxide nanoparticles onto the MWNT support. These samples were labeled "P-samples." All of the samples were characterized by TPR and TEM measurements and tested in CO hydrogenation. TPR measurements showed easy reducibility of the metal ions in the I-Co and I-Fe samples. TEM images generally pointed to a rather uniform particle size both before and after the reaction. The highest catalytic activity and high selectivity toward C_2–C_4 and C_{5+} fractions, as well as for olefin formation, were found for I-Fe. Catalytic activity was lower for P-Co and P-Fe. It can be established that these novel catalyst systems have high activity with high olefin selectivity and high fractions of larger hydrocarbons.

Keywords: Multiwall carbon nanotubes; Co and Fe on carbon nanotubes; CO hydrogenation; Electron microscopy; TPR

1. Introduction

Research activity focusing on the development of Fischer–Tropsch catalysts covers a widening field, even encompassing support materials. After the exhaustively investigated silica, alumina, titania, and mixed oxides, a new, challenging material, carbon nanotubes (CNTs), appeared as a possible support for various catalytic applications [1,2]. Studies comparing the catalytic activity of metal catalysts supported on various oxides, amorphous carbon, and CNTs showed that catalytic performance was generally the best on CNTs. For example, a multiwall CNT (MWNT)-supported platinum catalyst showed superior activity in catalytic wet air oxidation of nitrogen-containing compounds [3], and CNT-supported platinum catalyst did so in the oxidation of environmentally harmful organic compounds to CO_2 [4]. Yin et al. showed that CNT-supported metals are active in hydrogen generation from ammonia and that the CNT-supported Ru exhibited the highest efficiency in the reaction [5]. Chen et al. found that potassium-doped ruthenium supported on MWNTs gave the highest yield in ammonia synthesis among the potassium-doped ruthenium catalysts supported on various carbon materials [6]. Similar observations were published by Niesz et al., who reported that purified MWNT-supported platinum catalyst showed the highest turnover frequency in isopropanol dehydrogenation [7]. A recent review article discusses the development of the role of CNTs in heterogeneous catalysis between 1990 and 2003 [8].

The deposition of catalytic components onto CNTs—in most cases, onto MWNTs—is also an intriguing problem, as can be seen in the relevant literature. It is well known that the purification of catalytically made MWNTs is mainly performed in two steps; the first step is to remove the catalyst, where the

* Corresponding author.
E-mail address: konya@chem.u-szeged.hu (Z. Kónya).

0021-9517/$ – see front matter
doi:10.1016/j.jcat.2006.08.012

second step uses a strong oxidative media to remove amorphous carbon [9]. Generally, these treatments result in nanotube samples free of amorphous carbon and nontubular carbon nanostructures. This process also involves the generation of oxygen-containing functional groups on the outer shells of the nanotubes, however. These functional groups can help bond metal nanoparticles onto the nanotube surface [10,11]. Electrochemical deposition of metal particles with uniform size distribution has also been reported [12–14].

The metal or metal oxide nanoparticles-decorated carbon nanostructures can be used as catalysts for various catalytic reactions because of the strong metal–support interaction due to the graphitic nature of CNTs [15]. Iijima et al. reported a direct route for deposition of Pd nanoclusters with an average diameter of 2.3 nm on single-walled carbon nanohorns in a one-step reaction [16,17]. Zhang et al. reported on palladium nanoparticles filling the CNTs and their application in hydrogenation of benzene [18]. Palladium nanoparticle–filled MWNTs were used as selective catalysts for hydrogenation of cinnamaldehyde to hydrocinnamaldehyde [19]. CNTs have high thermal stability [20,21] and, similar to graphite, high resistance against various corrosive chemicals. These characteristics make this type of nanoporous material a nanoreactor in which chemical reactions may take place; due to the restricted reactor volume, some sort of shape selectivity is expected. Nhut et al. gave a nice example of the use of CNTs as a nanoreactor [22]; they used the system for several interesting transformations, including the decomposition of H_2S and the production of one-dimensional zeolite crystals.

The catalytic activities, the stability of the catalysts and the product selectivity of a series of Fe/CNT catalysts in Fischer–Tropsch synthesis have been investigated [23]. Iron supported on CNTs produced a very stable and active catalyst. The addition of potassium led to decreased hydrogenation activity and increased chain growth during the Fischer–Tropsch reaction, producing higher-molecular weight products. The production of C_2 olefins also increased. Potassium also decreased methane production and increased water–gas shift activity. Copper, introduced to facilitate reduction of the iron, increased the Fischer–Tropsch synthesis reaction rate but had no major effect on the product spectrum.

The main goal of the present work is to prepare MWNT-supported cobalt and iron catalysts using two different preparation methods—a conventional impregnation–heat treatment reduction method and deposition of preprepared metal oxide nanoparticles followed by reduction—and to characterize them using TPR and TEM and study the catalytic activity as well as selectivity in CO hydrogenation.

2. Experimental

2.1. Synthesis of MWNTs

MWNTs were produced by catalytic chemical vapor deposition (CCVD) of acetylene over alumina-supported iron–cobalt bimetallic catalyst [9]. The catalyst was placed onto a quartz boat positioned in the heating part of the quartz reactor tube, and nitrogen was introduced into the reactor while the temperature was increased up to 700 °C. At this temperature, 30 cm^3/min acetylene was mixed into the nitrogen stream (270 cm^3/min). The chemical decomposition of acetylene took place under these conditions. After 30 min, the generation of MWNTs was completed; the acetylene stream was shut off, and the reactor was cooled in nitrogen flow. The raw product was suspended in NaOH solution to remove the alumina, followed by washing with distilled water. The metal catalyst particles formed at the beginning of the synthesis procedure were dissolved in diluted acid solution. The amorphous carbon species generally accompanying CNT generation was oxidized using potassium permanganate in acidic media as described elsewhere [9]. Finally, the sample was washed with distilled water until neutral pH was reached and dried in air. The sample prepared by this procedure comprised high-grade CNTs containing only traces of metal impurities occluded inside the tubes. The specific surface area of the MWNT sample was 170 m^2/g. It is noteworthy that the surface area of the samples did not change significantly during TPR and catalytic treatments

2.2. Preparation of the metal/MWNT catalysts

Two types of catalysts were prepared using MWNTs as support. For the first group of samples, a simple impregnation method was used to deposit the metal precursors (iron and cobalt acetates) onto the MWNT support. The predetermined amount of metal salts was dissolved in distilled water, and a precalculated amount of MWNTs was added to the solutions during sonication. After 15 min of sonication, the solvent was removed, and the product was dried and crushed carefully in an agate mortar. These samples are labeled I-Co and I-Fe. The nominal compositions of these samples are summarized in Table 1.

The second family of the MWNT-supported metal catalysts was prepared in two steps, with the samples denoted as P-Co and P-Fe. First, the metal nanoparticles were synthesized using the oleate method described previously [24]. In short, this preparation method involves the following steps: Metal chloride is transformed to metal oleate in a reaction with sodium oleate. Metal oleate is decomposed in a high-boiling point solvent such as 1-octadecene. After the metal oxide nanoparticles are separated and redispersed in ethanol, they are deposited onto the MWNT support from the suspension. Cobalt and iron oxide nanoparticles were prepared. The nominal compositions of the samples are given in Table 1.

Table 1
Composition of supported metal oxide catalyst precursor samples

Sample	Precursor metal salt	Amount of metal salt (g)	Amount of MWNT (g)	Nominal metal concentration (w%)
I-Co	Co-acetate	0.422	1.9	5
I-Fe	Fe-acetate	0.311	1.9	5
P-Co	Co-oleate	0.471	1.0	2.5
P-Fe	Fe-oleate	0.447	1.0	2.5

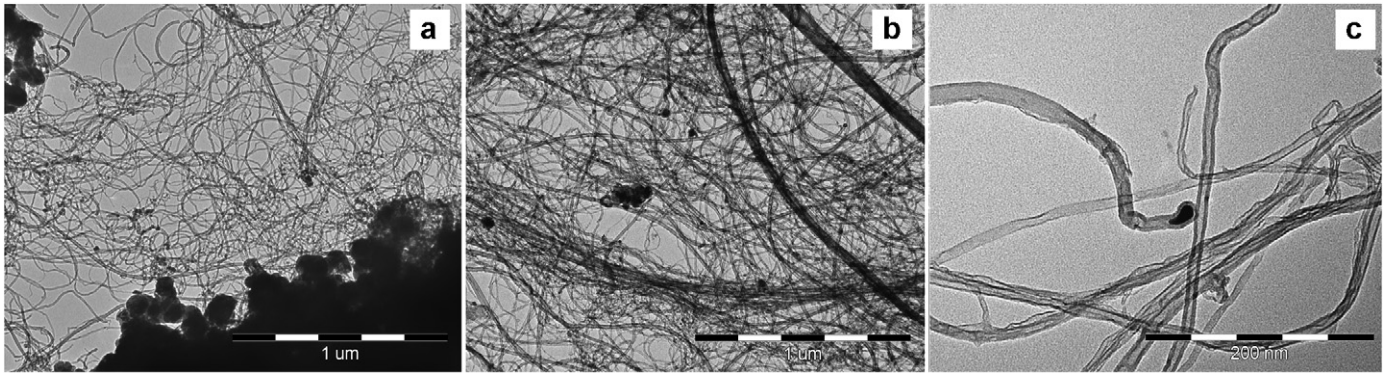

Fig. 1. TEM images of the support material: (a) as prepared MWNTs, (b) MWNTs after purification and before loading with metal precursors, (c) higher resolution image showing the encapsulated metal particles on the tube.

2.3. Characterization of the catalyst samples

The morphology of samples was characterized by transmission electron microscopy (TEM). Sample specimens for TEM studies were prepared by ultrasonic dispersion of the catalysts in distilled water, and the suspensions were dropped onto a carbon-coated copper grid. TEM investigations were carried out using a Philips CM20 (200 kV) transmission electron microscope equipped with a NORAN energy-dispersive spectrometer with a germanium detector. Several TEM micrographs were recorded for each sample and analyzed for particle size distribution using the ImageJ image analysis software [25]. At least 100 metal nanoparticles per sample were analyzed to determine their size and chemical composition.

Nitrogen adsorption measurements were carried out at 77 K with a Quantachrome Instruments NOVA 2000, and the BET surface area and the pore size distribution were determined from the isotherms.

The samples were characterized by temperature-programmed reduction (TPR) in a flow system using 1 vol% hydrogen/argon mixture with 10 °C min^{-1} temperature ramp with a flow rate of 30 cm^3 min^{-1}.

CO hydrogenation was carried out in a plug-flow reactor at 10 bar pressure and with a 2:1 mixture of H_2/CO using a flow rate of 15 cm^3 min^{-1}. The samples were pretreated in various ways, followed by reduction at 500 °C for 2 h. The products of reaction were analyzed by gas chromatography (CHROMPACK CP 9002, 50-m long plot fused silica column [0.53 mm i.d.] with a stationary phase of CP-Al_2O_3/KCl) with a temperature program.

The rate of CO hydrogenation (using 100 mg of catalyst and a 15 cm^3 min^{-1} flow rate, expressed in mol h^{-1} g^{-1}) is defined as the number of moles of CO converted per unit time per gram of catalyst. Product selectivity (S) is reported as the percentage of CO converted into a given product expressed in C atoms, excluding CO_2. $S(C_n)$ and $S(C_{5+})$ refer to the selectivity in hydrocarbons with n carbon atoms and to the selectivities of all hydrocarbons in the gas phase with a carbon atom number $\geqslant 5$.

3. Results and discussion

3.1. Morphology of the catalyst samples

TEM images of the parent MWNT sample show well-graphitized nanotubes with high aspect ratios. In some cases, metal particles were also detected, as shown in Fig. 1. These metal particles were encapsulated in the nanotubes during the synthesis procedure. Most likely these metal moieties do not interfere with the activity of the supported metal catalyst samples, because their concentration is very low. This is supported by the activity in CO hydrogenation (see Fig. 7).

For the two P samples, where the metal oxide nanoparticles were deposited onto MWNTs, TEM investigations were carried out to follow the different steps of the preparation. As can be seen in Fig. 2a, small iron oxide nanoparticles were formed on decomposition of the iron oleate. The histogram in the inset of the figure reveals a narrow particle size distribution centered at 6 nm. These tetrahedral-shaped particles were deposited on the MWNTs under sonication. Fig. 2b shows that the nanoparticles were not located separately; most of them formed aggregates consisting of numerous particles. For cobalt oxide, much bigger particles were formed. The average size was around 200 nm, as shown in the TEM image and the inset in Fig. 3.

The metal acetate, finely dispersed on the MWNTs, can be decomposed by heat treatment (for the I-Fe and I-Co samples). The metal oxide thus formed was reduced either ex situ in a separated reactor under various conditions using different gases or in situ in the catalytic reactor, where the reacting mixture acts as a reducing agent in the initial minutes of the reaction. The shape and size of nanoparticles formed in the reduction are displayed in Fig. 4. It is seen that rather uniform nanoparticles without any dominant shape were formed.

3.2. TPR experiments

The reducibility of the calcined precursors was investigated by TPR. These experiments determined the appropriate reduction temperature for the catalyst pretreatments. Three different TPR experiments were carried out. The first set of experiments

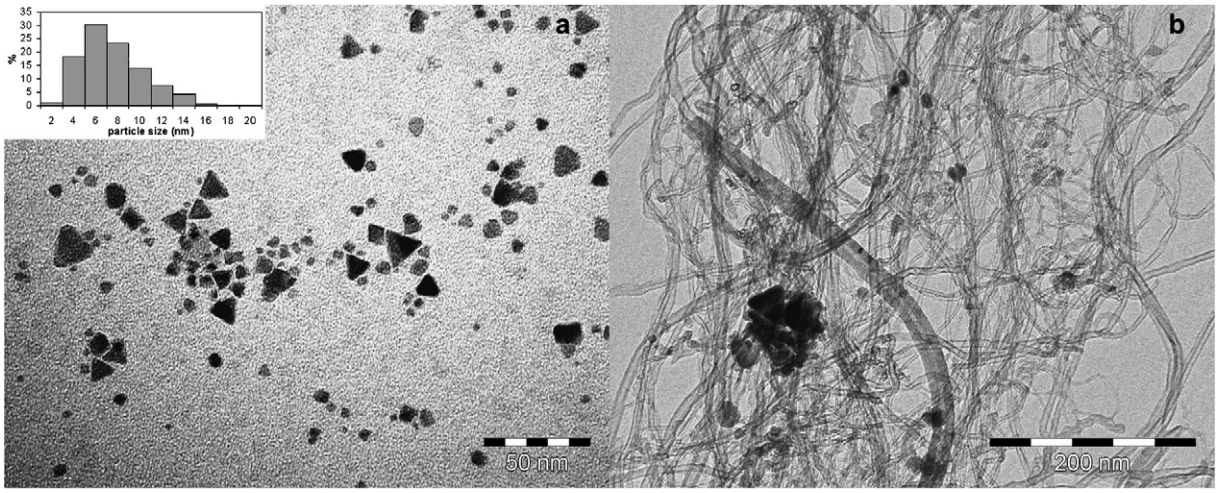

Fig. 2. TEM images showing the iron oxide nanoparticles dispersed in ethanol (a) and supported on MWNTs (b). The inset in part (a) reveals the particle size distribution of iron oxide nanoparticles.

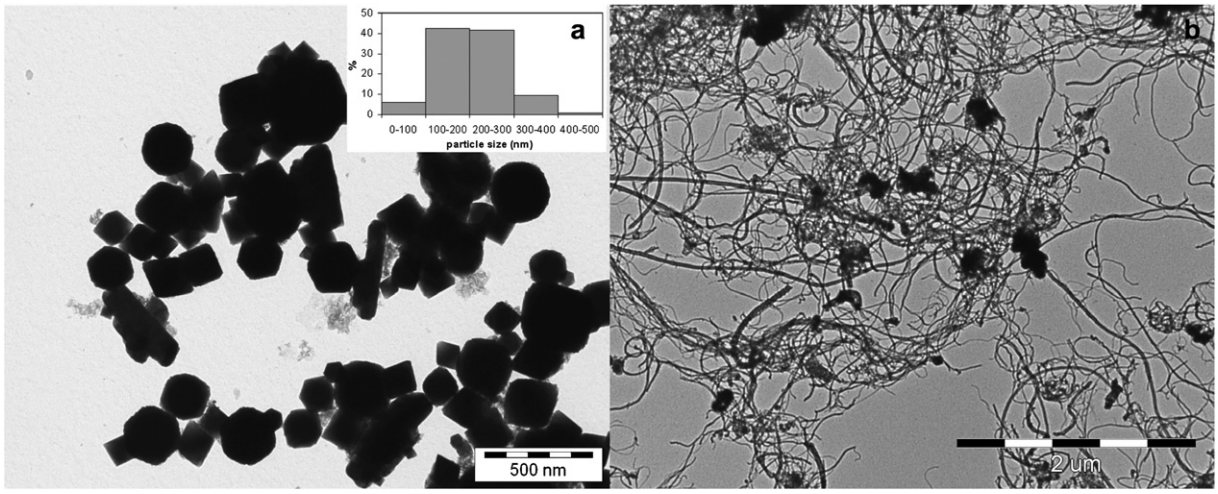

Fig. 3. TEM image of Co oxide nanoparticles dispersed in ethanol (a) and MWNTs loaded with Co oxide nanoparticles (b). The inset in part (a) reveals the particle size distribution of cobalt oxide nanoparticles.

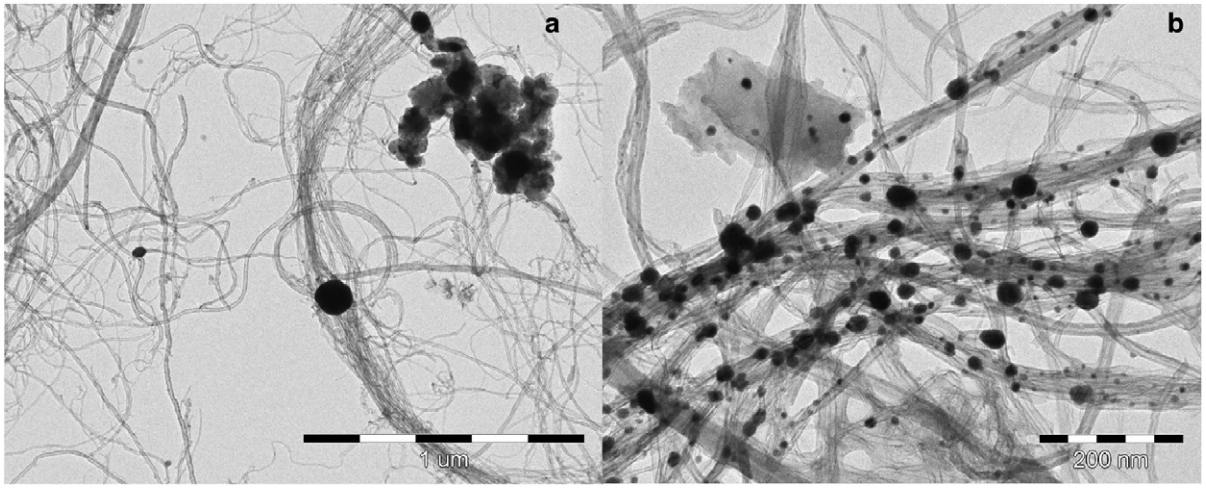

Fig. 4. TEM images of metal nanoparticles on MWNT supports formed after TPR of impregnated samples: (a) I-Fe after TPR, (b) I-Co after TPR.

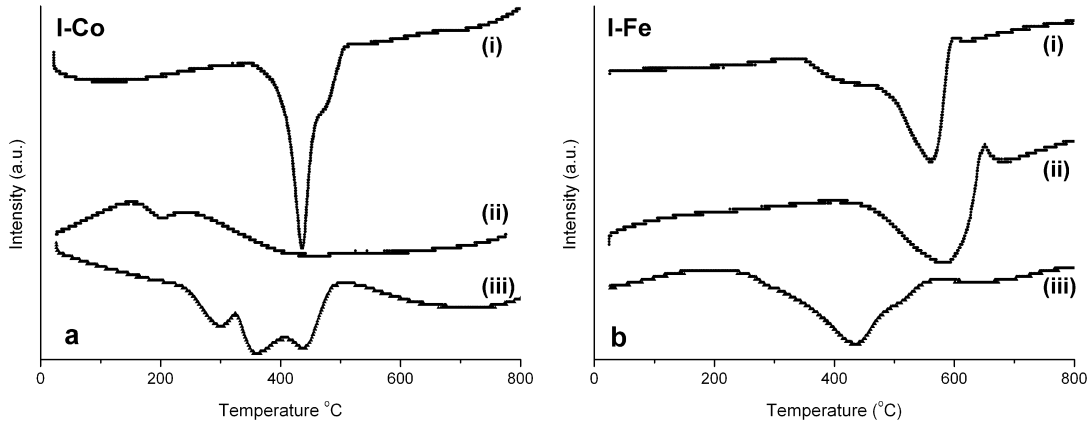

Fig. 5. TPR curves of I-Co and I-Fe samples: (i): TPR curves of Co and Fe acetate-loaded samples, (ii): TPR curves of Co and Fe acetate-loaded samples after acetate decomposition in He at 600 °C, (iii): TPR curves of Co and Fe acetate-loaded samples after acetate decomposition in O_2 at 300 °C.

investigated the catalyst precursors, the cobalt acetate- and iron acetate-loaded samples (I-Co and I-Fe, respectively). The TPR spectrum of the cobalt acetate-loaded sample showed a well-defined reduction peak at 435 °C [see Fig. 5a, curve (i)]. For the iron acetate-loaded sample, the TPR profile showed a main peak at 565 °C and a shoulder on the lower-temperature side at around 440 °C [Fig. 5b, curve (i)]. The analysis of effluent gases CO and CO_2 were identified by quadrupole mass spectrometry (QMS). These are the products of acetate decomposition. The hydrogen uptake for the cobalt loaded as a prepared sample was 475 μmol g_{cat}^{-1}.

In the second set of TPR experiments, the impregnated cobalt or iron samples (I-Co and I-Fe, respectively) were reduced after decomposition of acetate in He at 600 °C. Fig. 5a, curve (ii) shows the TPR profile for the cobalt-containing sample. Compared with the first set of experiments, the shape of the TPR curve completely changed, and a small and a very broad peak appeared. Determining the precise temperature maximum of these peaks was difficult. The approximate temperatures were 200 and 450 °C. The hydrogen uptake for this sample was 570 μmol g_{cat}^{-1}. The TPR peak for the iron-containing sample was centered at 570 °C, as can be seen in Fig. 5b, curve (ii).

In the third type of experiment, the acetate was decomposed first in oxygen at 300 °C before the reduction experiment. Fig. 5a, curve (iii) shows three peaks at 300, 360, and 435 °C. It is assumed that during oxygen treatment, various form of cobalt oxides are formed that can be reduced at different temperatures. In contrast, only one TPR signal was observed for the iron-containing sample at 440 °C [Fig. 5b, curve (iii)]. This temperature is significantly lower than that found for the iron-containing sample pretreated in He or reduced without any pretreatment. The hydrogen uptake for the oxygen-treated sample was 538 μmol g_{cat}^{-1}. The difference in hydrogen uptake in the cobalt and iron cases was about 10% between the samples pretreated in different procedures, which is within the range of accuracy.

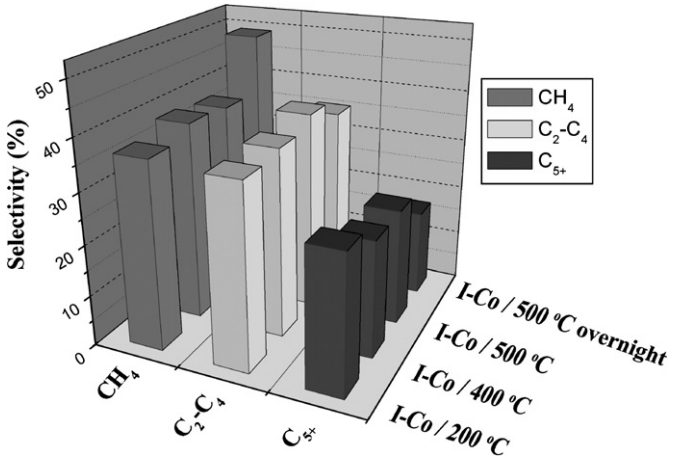

Fig. 6. Selectivities in CO hydrogenation over I-Co samples pretreated at different temperatures. The reaction temperature was 234 °C in each experiment.

3.3. CO hydrogenation

3.3.1. Influence of pretreatment

Investigation of the influence of reduction temperature with sample I-Co showed that in CO hydrogenation performed at 234 °C, the volume of C_{5+} fraction decreased significantly, whereas formation of the C2–C4 fraction increased slightly as the temperature of pretreatment was raised from 200 to 500 °C, as shown in the block diagram in Fig. 6.

Conducting the reaction at 234 °C overnight, changes were observed in both the conversion and the selectivity of the reaction. An approximate fourfold decrease in the rate of reaction measured at 234 °C was seen. From this, it follows that the catalyst was stabilized in the reaction. This effect may be due to the increased size of cobalt particles; a similar effect was recently reported in methane conversion over a Co/Al_2O_3 sample [26].

3.3.2. Influence of reaction temperature

Fig. 7 displays the rates over all five samples. Surprisingly, the I-Fe sample appears to be the most active catalyst, followed

Table 2
The initial rate (r_0 in mol s^{-1} g_{cat}^{-1}), the Anderson–Schulz–Flory α-value, the olefin selectivity ($C^{=}/C^{-}+C^{=}$) and the activation energy (E_{act}) for I-Co, I-Fe, P-Co and P-Fe samples in CO hydrogenation reaction

Sample	Treatment	[1]r_0 (mol s^{-1} g_{cat}^{-1})	[2]α	Olefin selectivity	E_{act} (kcal mol^{-1})
	H_2/1 h at 500 °C	1.6×10^{-7} (at 234 °C)	–	–	–
I-Co 21.3 mg	H_2 overnight at 200 °C	1.5×10^{-7} (at 234 °C)	0.64	0.88	–
	H_2/2 h at 500 °C after 50 min	1.3×10^{-7} (at 234 °C)	–	–	–
	H_2 overnight at 234 °C	1.6×10^{-7} (at 234 °C)	0.64	0.85	29
I-Fe 29.0 mg	H_2 at 400 °C + H_2 at 200 °C overnight	2.5×10^{-6} (at 252 °C)	0.72	0.88	25
P-Co 25.6 mg	H_2 at 400 °C/2 h + H_2/1 h at 500 °C	6.1×10^{-8} (at 251 °C)	0.50	0.90	–
P-Fe 25.7 mg	H_2 at 500 °C + H_2 at 250 °C overnight	4.8×10^{-8} (at 251 °C)	0.56	0.93	23
	+ H_2 at 300 °C 90 min	1.4×10^{-7} (at 275 °C)	0.55	0.93	–

[1] r_0 is the initial rate, the negative of the slope of the curve of reactant concentration versus time at $t = 0$. It was determined by a graphic method.
[2] $\alpha = r_p/(r_p + r_t)$, where r_p and r_t are respectively the rates of propagation and termination.

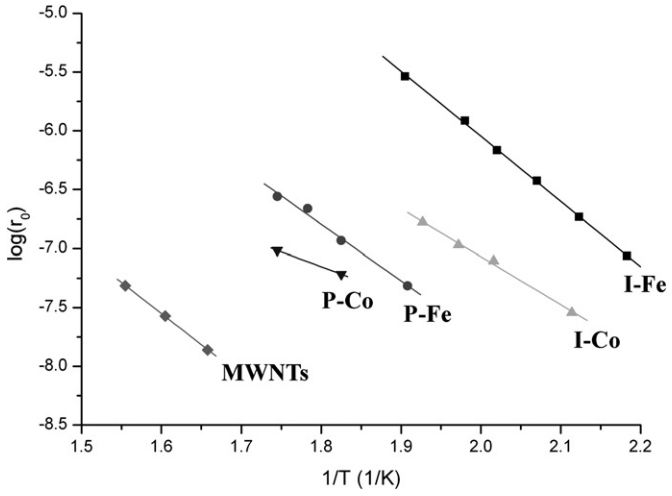

Fig. 7. Logarithm of the initial rate vs reciprocal temperature for pure MWNT, I-Co, I-Fe, P-Co and P-Fe samples.

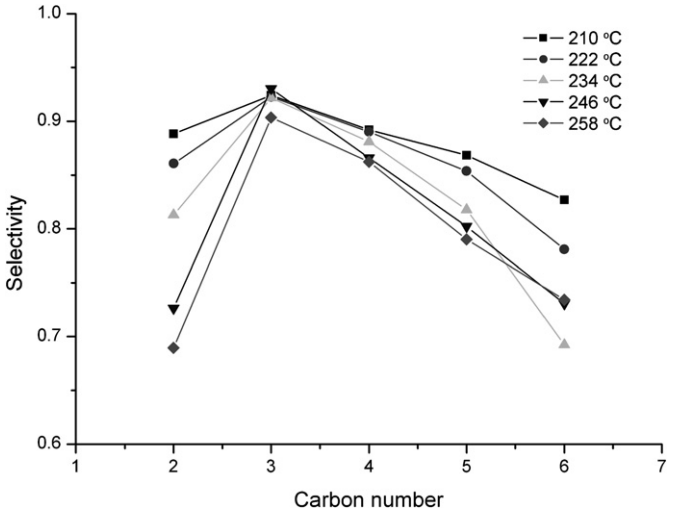

Fig. 8. Olefin selectivity vs carbon number in CO hydrogenation performed on I-Co catalyst at different temperatures indicated by the signs.

by I-Co. Table 2 gives the initial rates, the Anderson–Schulz–Flory α-value [$\alpha = r_p/(r_p + r_t)$, where r_p and r_t are the rates of propagation and termination, respectively], the olefin selectivity, and the Arrhenius parameters. For all samples, olefin selectivity [$C^{=}/(C^{=} + C^{-})$] was high, and the values did not change drastically in the applied temperature range. Fig. 8 gives a typical set of data on olefin selectivity versus the carbon number derived from the measured data over the I-Co catalysts at different temperatures. A slight decrease occurred toward higher hydrocarbons, but the average value was around 0.85. The α value was highest for the I-Fe sample prepared from an acetate precursor; for the other samples, this value varied in the range of 0.5–0.65.

Fig. 9 plots the CH_4, C_2–C_4, and C_{5+} selectivities. The diagrams reveal reverse selectivity profiles for methane for the I-Fe and I-Co catalysts. For I-Co, methane selectivity was high and showed the highest values for the reactions occurring at various temperatures. C_2–C_4 selectivity changed only moderately with reaction temperature, but C_{5+} selectivity decreased sharply with reaction temperature. In contrast, on I-Fe, methane selectivity was the lowest at each reaction temperature, and C_2–C_4 as well as C_{5+} selectivity were the highest. This finding can be explained by the predominating chain propagation toward higher hydrocarbons for the iron-containing sample.

Fig. 10 shows two sets of experimental data. These results were obtained with the catalyst produced by the two-step method; that is, the metal oxide nanoparticles were deposited on the MWNT support. For the P-Fe sample, the methane selectivity measured at 275 °C was the highest not only in this experimental set, but also considering each catalyst tested. With increasing reaction temperature, methane selectivity decreased slightly and C_2–C_4 selectivity increased moderately. Over the P-Co catalyst at increasing temperatures, C_2–C_4 selectivity significantly exceeded methane selectivity.

3.4. Morphology of the used catalysts

As shown in Fig. 11, the particle size distributions of metal nanoparticles remained uniform even after the reaction; the TEM images reveal only slight changes in particle size. The rather small particles did not aggregate significantly during the reaction. The nanoparticles on P-Co and P-Fe preserved their sizes; that is, the cobalt particles in P-Co remained large, and the iron particles in P-Fe were small even after the reaction. An

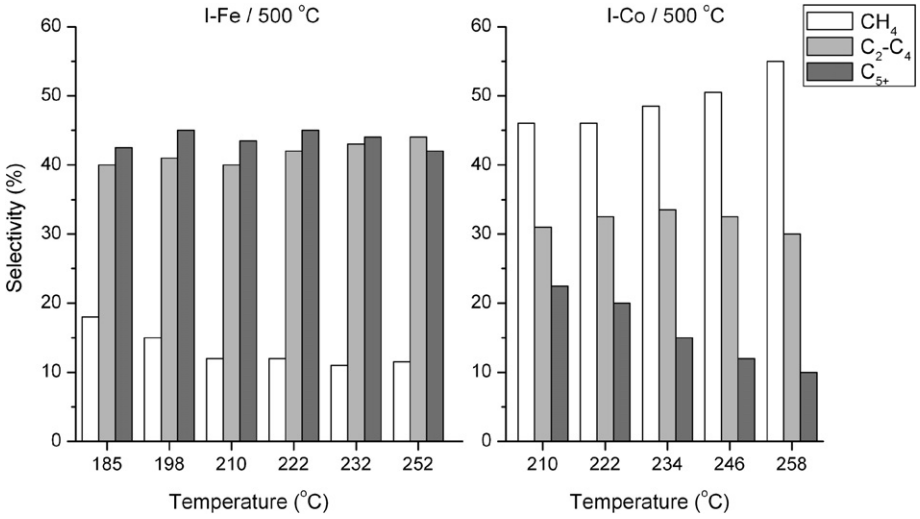

Fig. 9. Selectivity of CH_4 (white column), C_2–C_4 (gray column) and C_{5+} (black column) on I-Fe (a) and I-Co (b) samples.

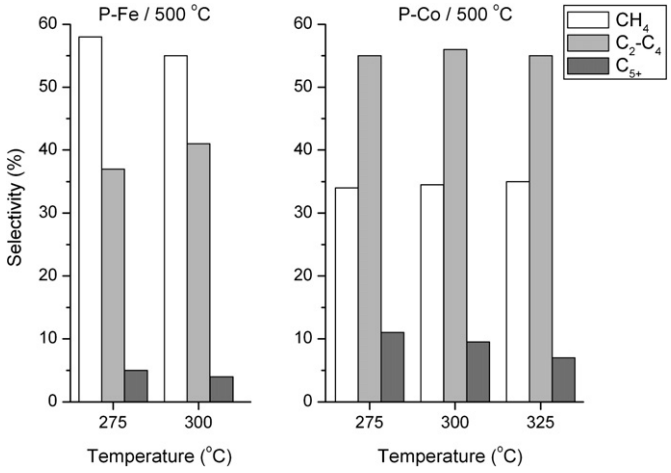

Fig. 10. Selectivity of CH_4 (white column), C_2–C_4 (gray column) and C_{5+} (black column) on P-Fe (a) and P-Co (b) samples.

alternative explanation for the observed particle sizes in P-Co could be that some sort of nanoparticle dispersion occurred during the reaction, because the particles on the reduced sample could be aggregated from very small particles. However, the spent P-Co catalyst showed rather uniform, well-dispersed, large cobalt particles.

In contrast, in the I-Fe sample, reduction of the catalyst precursor generated by decomposition of iron acetate on the MWNT support resulted in the formation of rather large metal particles (see Fig. 4a), which became smaller after reaction (see Fig. 11a). This may explain the very high activity and high selectivity for C_{5+} hydrocarbons. The particle size effect in Fe-containing catalysts remains a very interesting question [27]. Vannice et al. investigated that the turnover frequency (TOF) for CO hydrogenation on large and small iron particles and found that the TOF is much higher on large metal particles than on small particles [28]. Results obtained by Mossbauer spectroscopy showed that the larger Fe particles were about 90% carbided to ε'-carbide, whereas the smaller particles were only partially converted. In summary, our findings indicate that the particle size effect is influenced to an uncertain degree by the changing nature of the iron carbide formation.

It is well known that selectivity is a result of the propagation of chain growth and chain termination, which has been evidenced in Re–Co/Al_2O_3 and Ru–Co/Al_2O_3 bimetallic samples [29]. On I-Fe, chain growth was much faster; that is, longer chains were formed.

Blank reactions (CO hydrogenation) were performed on purified MWNT unloaded with any metal precursor, under the reaction conditions used for the general catalytic runs. The main product formed at a very low conversion level was methane (80% in the gas product), with almost no higher hydrocarbons formed. These data suggest that the traces of cobalt or iron particles left behind in MWNT synthesis and embedded inside the tubes are almost nonaccessible for the reactant CO and hydrogen. This is an important finding demonstrating that care must be taken to ensure that the sources of the materials are adequately described and characterized when using MWNTs as catalyst supports. It is important to note that the catalytic activity for a catalyst supported on MWNTs is in agreement with Coville's findings [30]. Rodriguez et al. introduced an active phase (e.g., FeCu) onto CNFs via an incipient wetness technique [31] and found that the FeCu/CNF catalysts displayed a high activity for ethylene hydrogenation. The authors ascribed this high activity to a unique (metal–support) interaction. Unfortunately, no characterization data was provided to explain the observed activity differences.

In our case, the high activity and selectivity of the tested catalysts can be divided into two groups. The samples prepared from acetate precursors were well dispersed after decomposition of acetate salts in He up to 600 °C, and well-defined TPR peaks were obtained. The TEM images indicated that some sort of disaggregation or dispersion occurred during the CO hydrogenation reaction. The large particles or particle agglomerates were more active in the formation of longer chains; as the particles became smaller, the catalytic activity may have leveled off. For the I-Co catalyst, the particle size distribution did not change during the reaction, as shown by the TEM images ob-

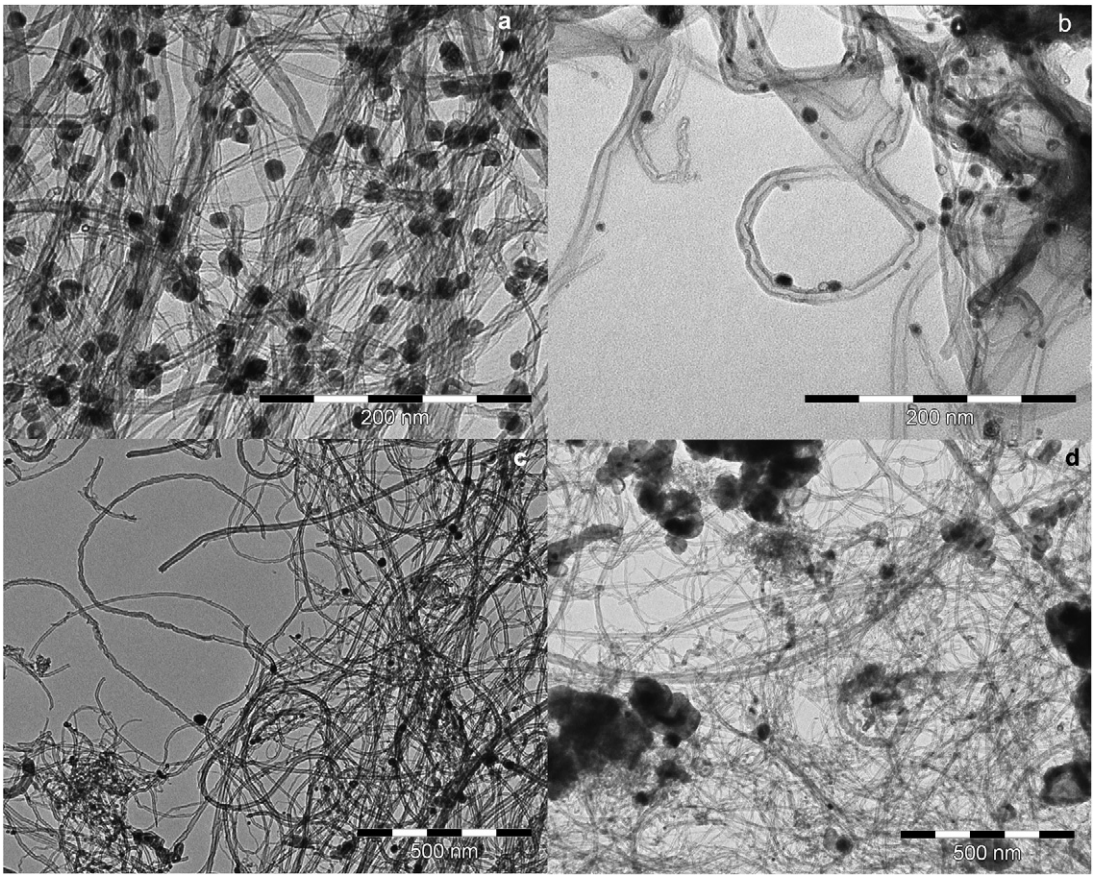

Fig. 11. TEM images of nanoparticles after reaction: (a) I-Fe; (b) I-Co; (c) P-Fe; (d) P-Co.

tained before and after the catalytic run. From this, it follows that significant change in either catalytic activity or selectivity due to the size of particles would not be expected. This was our finding. On the other hand, the P-Co and P-Fe samples, which were prepared by deposition of presynthesized metal oxide nanoparticles, exhibited a very low hydrogen uptake on TPR. These samples had lower activities than the impregnated I-Co or I-Fe catalysts.

As mentioned earlier, surface hydrogen concentration affects selectivity. In addition to the argument given above, the secondary effect of hydrogen is to keep the surface "clean," preventing the formation of nonactive carbonaceous deposits. This action was better fulfilled on the I-Co and I-Fe samples than on the P-samples. This factor may have contributed to the higher selectivity, because the propagation of hydrocarbon chain growth progresses faster on the I-samples, leading to C_2–C_4 and C_{5+}.

4. Conclusion

CO hydrogenation was investigated over Co or Fe catalysts supported on MWNTs synthesized by CCVD of acetylene over supported iron–cobalt bimetallic catalysts deposited on freshly precipitated alumina. The catalysts for CO hydrogenation were prepared by a simple impregnation method with a metal acetate precursor (I-Fe and I-Co) or metal oxide nanoparticles (P-Fe and P-Co) suspended in oleate using MWNTs as support. The samples were characterized by TPR and TEM measurements and tested in the CO hydrogenation. The TPR measurements showed easy reducibility of the I-Co and I-Fe samples. I-Fe showed the highest catalytic activity and high selectivity toward C_2–C_4 and C_{5+} fractions as well as for olefin formation. The Co-containing catalyst promoted the formation of these fractions to a lesser extent, but it was affected by the pretreatment (reduction temperature, treatment in He or in O_2).

The Co and Fe catalysts prepared from oleate suspension of cobalt and iron oxide nanoparticles showed lower catalytic activity. This was likely due to the limited oxide reducibility of the metal particles in hydrogen. It is very likely that the reduction did not proceed to completion in the bulk phase even the particle sizes were very small. Furthermore, the surface of the metal nanoparticles may have contained oxide spots, hindering the formation of clean metal surfaces.

It can be established that these novel catalyst systems show high activity with high olefin selectivity and high fractions of larger hydrocarbons.

Acknowledgments

The authors are indebted to the National Science and Research Fund (OTKA T-034920 and T-049078). Z. Kónya acknowledges financial support from the Bolyai Janos Research Fellowship.

References

[1] W. Li, C. Liang, W. Zhou, J. Qui, Z. Zhou, G. Sun, Q. Xin, J. Phys. Chem. B 107 (2003) 6292.
[2] M. Carmo, V.A. Paganin, J.M. Rosolen, E.R. Gonzalez, J. Power Sources 142 (2005) 169.
[3] J. Garcia, H.T. Gomes, P. Serp, P. Kalck, J.L. Figueiredo, J.L. Faria, Catal. Today 102–103 (2005) 101.
[4] H.T. Gomes, P.V. Samant, Ph. Serp, Ph. Kalck, J.L. Figueiredo, J.L. Faria, Appl. Catal. B 54 (2004) 175.
[5] S.-F. Yin, Q.-H. Zhang, B.-Q. Xu, W.-X. Zhu, C.-F. Ng, C.-T. Au, J. Catal. 224 (2004) 384.
[6] H.-B. Chen, J.-D. Lin, Y. Cai, X.-Y. Wang, J. Yi, J. Wang, G. Wei, Y.-Z. Lin, D.-W. Liao, Appl. Surf. Sci. 180 (2001) 328.
[7] K. Niesz, A. Siska, I. Vesselenyi, K. Hernadi, D. Mehn, G. Galbacs, Z. Kónya, I. Kiricsi, Catal. Today 76 (2002) 3.
[8] Ph. Serp, M. Corrias, Ph. Kalck, Appl. Catal. A 253 (2003) 337.
[9] Z. Kónya, NATO Sci. Ser. E 372 (2001) 85.
[10] Z.-J. Lin, Z.-Y. Yuan, W. Zhou, L.-M. Peng, Z. Xu, Phys. Chem. Chem. Phys. 3 (2001) 2518.
[11] R. Giordano, Ph. Serp, Ph. Kalck, Y. Kim, J. Schreiber, Ch. Marhic, J.-L. Duvail, Eur. J. Inorg. Chem. (2003) 610.
[12] D.J. Guo, H.L. Li, Carbon 43 (2005) 1259.
[13] Y. Xing, J. Phys. Chem. B 108 (2004) 19255.
[14] C.-L. Sun, L.-C. Chen, M.-C. Su, L.-S. Hong, O. Chyan, C.-Y. Hsu, K.-H. Chen, T.-F. Chang, L. Chang, Chem. Mater. 17 (2005) 3749.
[15] P. Tribolet, L. Kiwi-Minsker, Catal. Today 105 (2005) 337.
[16] S. Iijima, M. Yudasaka, R. Yamada, S. Bandow, K. Suenaga, F. Kokai, K. Takahashi, Chem. Phys. Lett. 309 (1999) 165.
[17] E. Bekyarova, A. Hashimoto, M. Yudasaka, Y. Hattori, K. Murata, H. Kanoh, D. Kasuya, S. Iijima, K. Kaneko, J. Phys. Chem. B 109 (2005) 3711.
[18] A.M. Zhang, J.L. Dong, Q.H. Xu, H.K. Rhee, X.L. Li, Catal. Today 93–95 (2004) 347.
[19] J.-P. Tessonnier, L. Pesant, G. Ehret, M.J. Ledoux, C. Pham-Huu, Appl. Catal. A 288 (2005) 203.
[20] J.F. Colomer, P. Piedigrosso, I. Willems, C. Journet, C. Bernier, G. Van Tendeloo, A. Fonseca, J.B. Nagy, J. Chem. Soc. Faraday Trans. 94 (1998) 3753.
[21] T. Kanyó, Z. Kónya, A. Kukovecz, F. Berger, I. Dekany, I. Kiricsi, Langmuir 20 (2004) 1656.
[22] J.-M. Nhut, L. Pesant, J.-P. Tessonnier, G. Wine, J. Guille, C. Pham-Huu, M.-J. Ledoux, Appl. Catal. A 254 (2003) 345.
[23] M.C. Bahome, L.L. Jewell, D. Hildebrandt, D. Glasser, N.J. Coville, Appl. Catal. A 287 (2005) 60.
[24] J. Park, K. An, Y. Hwang, J.-G. Park, H.-J. Noh, J.-Y. Kim, J.-H. Park, N.-M. Hwang, T. Hyeon, Nature Mater. 3 (2004) 891.
[25] W. Rasband, ImageJ 1.31v, A Public Domain Image Analysis Program for the Java Platform, National Institutes of Health, USA, 2003, http://rsb.info.nih.gov/ij.
[26] L. Borkó, L. Guczi, Top. Catal., DOI:10.1007/s11244-006-0035-4.
[27] M. Boudart, M.A. McDonald, J. Phys Chem. 88 (1984) 2185.
[28] H.-J. Jung, P.L. Walker, M.A. Vannice, J. Catal. 75 (1982) 416.
[29] L. Guczi, G. Stefler, L. Borkó, Zs. Koppány, F. Mizukami, M. Toba, S. Niwa, Appl. Catal. A 246 (2003) 79;
L. Guczi, Catal. Today 101 (2005) 53.
[30] M.C. Bahome, L.L. Jewell, D. Hildebrandt, D. Glasser, N.J. Coville, Appl. Catal. A 287 (2005) 60.
[31] N.M. Rodriguez, M.-S. Kim, R.T.K. Baker, J. Phys. Chem. 98 (1994) 13108.